Icarus 442 (2025) 116744

Contents lists available at ScienceDirect

Icarus

journal homepage: www.elsevier.com/locate/icarus

Lithologies of Dimorphos revealed by boulder morphological classes

F. Tusberti [a,*], M. Pajola [a], L. Penasa [a], A. Lucchetti [a], M. Massironi [b,c,a], G. Munaretto [a], J. Beccarelli [b,a], R. Pozzobon [b,d,c], C. Rossi [a], G. Poggiali [e], N. Murdoch [f], C.Q. Robin [f], A. Duchene [f], M. Amoroso [g], I. Bertini [h], J.R. Brucato [e], A. Capannolo [i], S. Caporali [e], M. Ceresoli [j], G. Cremonese [a], M. Dall'Ora [k], V. Della Corte [k], J.D.P. Deshapriya [l], E. Dotto [l], E. Mazzotta Epifani [l], I. Gai [m], E. Gramigna [m], P.H.A. Hasselmann [l], S. Ieva [l], G. Impresario [m], S. Ivanovski [n], R. Lasagni Manghi [m], M. Lavagna [j], M. Lombardo [m], D. Modenini [m], P. Palumbo [o], D. Perna [l], S. Pirrotta [g], A. Rossi [p], P. Tortora [m], M. Zannoni [m], G. Zanotti [j], A. Zinzi [g], B. Buratti [q], J.M. Trigo-Rodrigez [r], L. Gomez Casajus [m]

[a] INAF-OAPD Astronomical Observatory of Padova, vicolo dell'Osservatorio, 5, 35122 Padova, Italy
[b] Department of Geosciences, University of Padova, Padova, Italy
[c] CISAS, University of Padova, Padova, Italy
[d] Department of Physic and Astronomy, University of Padova, Padova, Italy
[e] INAF-Astrophysical Observatory of Arcetri, Firenze, Italy
[f] Institut Supérieur de l'Aéronautique et de l'Espace (ISAE-SUPAERO), Université de Toulouse, France
[g] Agenzia Spaziale Italiana, Roma, Italy
[h] Dipartimento di Scienze e Tecnologie, Università degli Studi di Napoli 'Parthenope', Napoli, Italy
[i] Purdue University, West Lafayette, IN, USA
[j] Dipartimento di Scienze e Tecnologie Aerospaziali, Politecnico di Milano - Bovisa Campus, Milano, Italy
[k] INAF - OACN Astronomical Observatory of Campodimonte, Napoli, Italy
[l] INAF - OAR Astronomical Observatory of Rome, Roma, Italy
[m] Dipartimento di Ingegneria Industriale, Alma Mater Studiorum - Università di Bologna, Forlì, Italy
[n] INAF- Osservatorio Astronomico di Trieste, Trieste, Italy
[o] INAF-Istituto di Astrofisica e Planetologia Spaziali, Roma, Italy
[p] IFAC-CNR, Firenze, Italy
[q] Jet Propulsion Laboratory, California Institute of Technology, CA, USA
[r] Institute of Space Sciences (CSIC/IEEC), Barcelona, Spain

ARTICLE INFO

Keywords:
Asteroids
Surfaces
Geological processes
Near-Earth objects
Satellites of asteroids

ABSTRACT

The stony/Sq-type binary system (65803) Didymos consists of two rubble pile bodies, Didymos, the primary, and its moonlet Dimorphos. In 2022, the first planetary defense mission Double Asteroid Redirection Test (DART) reached Dimorphos and collected unprecedented high-resolution images of its surface. They revealed a variegated surface completely covered by stacked boulders and cobbles with different shapes and textures. Their morphological heterogeneity likely reflects the lithologies originally present within the Didymos and Dimorphos' parent body, before its fragmentation.

We present a lithologic study of Dimorphos' surface, based on a morphological analysis of its boulders. Our approach considers each boulder's 2D outline, perceived 3D shape, and surface texture characteristics. Based on these features, we identified two main morphological classes. A total of 178 boulders were classified as *Angular morphology* covering 38.5 % of the mapped area. This type is characterized by cohesive boulders with straight and angular outlines as well as sharp three-dimensional edges, which form well-defined sub-planar facets. Additionally, the texture of this kind of rocks show low-to-mid *Roughness* and the presence of lineations on some boulders. On the other hand, 210 boulders were categorized as *Hummocky* morphology, which covers 61.5 % of the area. Such morphology appears more friable and features boulders with rounded shaped and ragged and irregular 2D perimeter. Their 3D perceived shape appears as flat-to-curve, with rough and hummocky surface textures due to embedded clasts. We interpret the *Hummocky* morphology as breccia lithology. On the other

* Corresponding author.
E-mail addresses: Filippo.tusberti@inaf.it, Filippo.tusberti@gmail.com (F. Tusberti).

https://doi.org/10.1016/j.icarus.2025.116744
Received 17 February 2025; Received in revised form 19 June 2025; Accepted 18 July 2025
Available online 19 July 2025
0019-1035/© 2025 The Authors. Published by Elsevier Inc. This is an open access article under the CC BY license (http://creativecommons.org/licenses/by/4.0/).

hand, although Angular morphology can be associated with multiple potential lithologies, we interpret it as either an achondritic/igneous lithology or a highly metamorphosed chondritic lithology. The breccias are likely characteristic of the parent body's outer layers, actively involved in impact and sedimentary processes. Conversely, the lithologies associated with the *An* morphology should represent deeper regions of the planetesimal, possibly exhumed by impacts. All these results will be further complemented by data from the Hera mission, which will arrive at (65803) Didymos system at the end of 2026.

1. Introduction

The growing interest in the Near Earth Asteroids (NEAs) has led to a new generation of space missions aimed at their exploration, such as the JAXA Hayabusa (Fujiwara et al., 2006) and Hayabusa 2 (Watanabe et al., 2017), the NASA Origins Spectral Interpretation Resource Identification Security Regolith Explorer (OSIRIS-REx, Lauretta et al., 2015, 2017), and the NASA Double Asteroid Redirection Test (DART, Rivkin et al., 2021) - ASI Light Italian Cubesat for Imaging of Asteroids (LICIACube, Dotto et al., 2021). These missions respectively studied the rubble-pile NEAs (25143) Itokawa, (162173) Ryugu, (101955) Bennu, and (65803) Didymos-Dimorphos, collecting a wealth of high-resolution data. In particular, meter to centimeter spatial scale images revealed varied and still-active asteroids' surfaces almost completely covered by heterogeneous rocks, boulders, and pebbles (Noguchi et al., 2010; Hirata et al., 2009; Jaumann et al., 2019; Jin and Bose, 2019; Lauretta et al., 2019; Barnouin et al., 2024; Bigot et al., 2024; Lucchetti et al., 2024; Pajola et al., 2024).

The DART mission was launched in November 2021 and reached the Didymos system roughly 10 months later (Chabot et al., 2024). This system is formed by two members classified as stony/Sq-type with a rubble pile structure (De León et al., 2006; Ieva et al., 2022; Pajola et al., 2022). Didymos is the primary member of the (65803) system and it has a size of 819x801x607 m, a top shape and an equatorial smoother bulge (Barnouin et al., 2024; Pajola et al., 2024; Zinzi et al., 2024). Dimorphos is the 177x174x116 m secondary moonlet, which has a uniform oblate spheroid shape (Barnouin et al., 2024), an estimated bulk density of $\sim 2400\,\mathrm{kg\,m^{-3}}$ and likely formed through rotational mass shedding and reaccumulation from Didymos (Raducan et al., 2024; Pajola et al., 2024).

The main objectives of the DART mission were to observe this binary asteroid and change the orbital period of Dimorphos by utilizing the spacecraft as a kinetic impactor (Rivkin et al., 2021). On 26 September 2022 DART successfully impacted Dimorphos' surface (Daly et al., 2023; Chabot et al., 2024) changing its orbital period by −33.24 min (Thomas et al., 2023; Scheirich et al., 2024; Naidu et al., 2024). The impact was observed by LICIACube (Dotto et al., 2021) and produced filamentary streams of ejecta that extended for several kilometers (Dotto et al., 2024; Deshapriya et al., 2023). Before the impact, Dimorphos was imaged with high-spatial resolution thanks to the Didymos Reconnaissance and Asteroid Camera for Optical navigation (DRACO, Fletcher et al., 2018). This camera revealed a varied surface completely covered by boulders, cobbles, and pebbles with different shapes, reflectance and texture (Barnouin et al., 2024). The morphological characteristics of the surface boulders of Dimorphos have been analyzed in detail and were found to be very similar to those on the surfaces of other rubble pile asteroids (Robin et al., 2024). Dimorphos' boulders also exhibit many interesting surface characteristics like impact structures, tumbling traces, thermal fatigue features and fractures (Barnouin et al., 2024; Bigot et al., 2024; Lucchetti et al., 2024).

Such variability of rocks has been also observed on other rubble piles' surfaces like the S-type Itokawa (Noguchi et al., 2010), and the B-type Bennu (Jawin et al., 2023), allowing lithological characterization of rocks. This type of investigation is of paramount importance to uncover insights into the geological processes that shaped the asteroid parent body and the differentiation stage at the moment of its catastrophic collision. Indeed, rubble-piles asteroids, like Didymos-Dimorphos, are thought to be formed as a result of the reaccumulation of debris generated by a catastrophic event that completely destroyed their planetesimal parent body (Fujiwara et al., 2006; Sugita et al., 2019; Agrusa et al., 2024). The various lithologies originally present on the parent body appear as morphologically heterogeneous rocks on the rubble pile asteroid.

In this work, we investigate the Dimorphos' lithologies by analyzing the geological and morphological characteristics of the boulders and cobbles present on its surface. Our findings provide new insight about the lithologies that could be present on the surface of an asteroid and the history and evolution of its parent body through the origin and formation processes of such lithologies.

2. Data and methods

2.1. Dataset

In order to identify the various lithologies present in the study area we chose the DRACO image with the highest possible spatial resolution. This image (dart_0401930049_43695_01_iof, Fig. 1) has been acquired by DRACO camera 1.818 s before the impact (Chabot et al., 2024) and has a pixel scale of 5.5 cm/px (Daly et al., 2023). We decided to exploit this image because it is sufficiently resolved to allow us to observe the morphological characteristics of boulders and cobbles (Robin et al.,

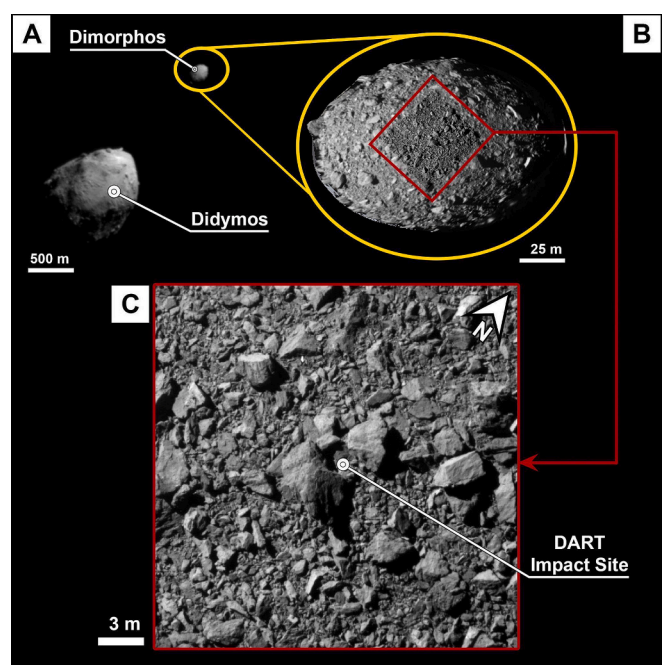

Fig. 1. A) The primary body Didymos and its moonlet Dimorphos captured by DRACO imager from a distance of 920 km about 2.5 min before the impact (Credit: NASA/Johnson Hopkins APL). B) A zoom in of Dimorphos shown with a mosaic of DRACO images. The red box corresponds to the image used in this work. North is up. C) A close up of the same image, where north is indicated by the white arrow and the white dot indicates the exact impact site of DART. (For interpretation of the references to colour in this figure legend, the reader is referred to the web version of this article.)

2024), facilitating the identification of the lithologies present in the area.

2.2. Methodology: morphological analysis

We manually identified each boulder and cobble larger than 0.4 m (41 px^2) and mapped them as polygons by drawing their outlines using the mapping tools of QGIS and established methods (Tusberti et al., 2024a, 2024b). Afterwards, we analyzed the boulders' characteristics in order to identify and assign to them a specific morphological class. Finally, we interpreted the lithologies corresponding to the observed morphologies and prepared the lithology map through the "Mappy" Qgis' plugin (Penasa et al., 2020). The shadows and the areas characterized by pebbles smaller than 0.4 m were also polygonized. However, we categorized them as "no data" to avoid any overinterpretation due to the small size of the pebbles and cobbles. This allowed us to know the exact surface of the image that has been analyzed.

Since no spectral or higher resolution data were available, we based the morphologic classes identification on five main morphological properties. *Angularity* and *Sinuosity* define the outline shape of the rock, while *Sharpness* describes its perceived 3D form. These properties are important because consistent and specific variations in rock shapes can be associated with differences in their mineralogical and physical characteristics (Panizza, 1996; Panizza and Goudie, 2013). Finally, *Roughness* and *Undulation* characterize the area of the rock just inside its boundary, defining their texture. Variations in grain-size, internal structure, and the way identical weathering processes (such as micro-impacts and thermal fatigue) have differently altered rocks are associated with changes in texture and cohesion (Colman, 1981; Carroll, 2012). At the scale of observation of this work, fine-grained rock (e.g. siltstone, mudstones or igneous rocks) will generally result in a macro-scale smoother and uniform surface texture (Kabeya and Legge, 1997). Conversely, coarse-grained rocks (e.g. coarse breccias and conglomerates) tend to have rougher and heterogeneous textures (Kabeya and Legge, 1997). Moreover, a very competent rock typically fractures into larger angular chunks (Carroll, 2012), while poorly competent or friable rocks are easily erodible and often produce rounded blocks with ragged outline (Colman, 1981; Carroll, 2012). For this reason, we also mapped fractures and lineations, to check if they can be linked with specific morphologies.

The five properties have been further classified into distinct levels, each manually assigned based on specific criteria detailed below.

i) *Angularity* refers to the presence of distinct, sharp angles in the general outline shape of the boulder. We classified as *low*, *medium,* and *high Angularity* the boulders based on how frequently their outline shows abrupt change of direction forming narrow angles (Fig. 2A, B). The *low* category includes those boulders with a regular outline and no narrow angles. The *medium* category contains boulders that show some sharp angles, but its general outline remains consistent. On the other hand, those boulders whose outline is totally defined by narrow angles have been categorized as *high Angularity*.

ii) *Sinuosity* is an additional parameter to describe the outline of the boulders. This is focused on the degree of curvature and irregularity of the rocks' boundaries. It represents how much the boulders' outline deviates from being straight, describing the complexity or irregularity of their perimeters (Fig. 2C, D). Rocks whose outlines are characterized by only a few asperities and deviations from the main pattern have been categorized as having *low Sinuosity*. The overall pattern of these outlines still appears consistent and regular. Conversely, the *High* category includes those outlines that are mainly composed of sinuous and irregular patterns with many asperities and ragged shapes.

iii) *Sharpness* property describes the perceived 3D shape of the boulder, specifically focusing on the presence of three-dimensional sharp edges. The presence of narrow, sharp, and acute three-dimensional edges was identified observing abrupt changes in the relative brightness of the rocks. These changes follow pronounced and straight patterns. Moreover, these edges are recognizable because they form distinguishable facets on the rock surface (Fig. 2E, F). Conversely, gradational changes in the relative brightness without any relevant pattern have been interpreted as curved and rounded surfaces. The *low Sharpness* category includes those boulders with a general flat shape without any relevant protrusion. *High Sharpness* indicates that the 3D perceived shape of the boulder is highly angular. Hence, it is characterized by the clear, well-defined acute angles and distinct, relatively flat facets formed by its three-dimensional edges. The *curved* category contains those boulders which show rounded and curved protrusion that characterize their general 3D perceived shape. Finally, the *medium* cathegory gathers all the boulders out from the endmembers.

iv) *Roughness* property describes the high-frequency asperities and irregularities of the boulders' surface at the scale of the image. This property is often associated with the degree of erosion and weathering the boulder has undergone, with more weathered rocks typically appearing rougher (Colman, 1981; Carroll, 2012). Moreover, it can be also linked with the grainsize of the rock. A fine-grained rock (e.g. phyllosilicates or effusive rocks) will

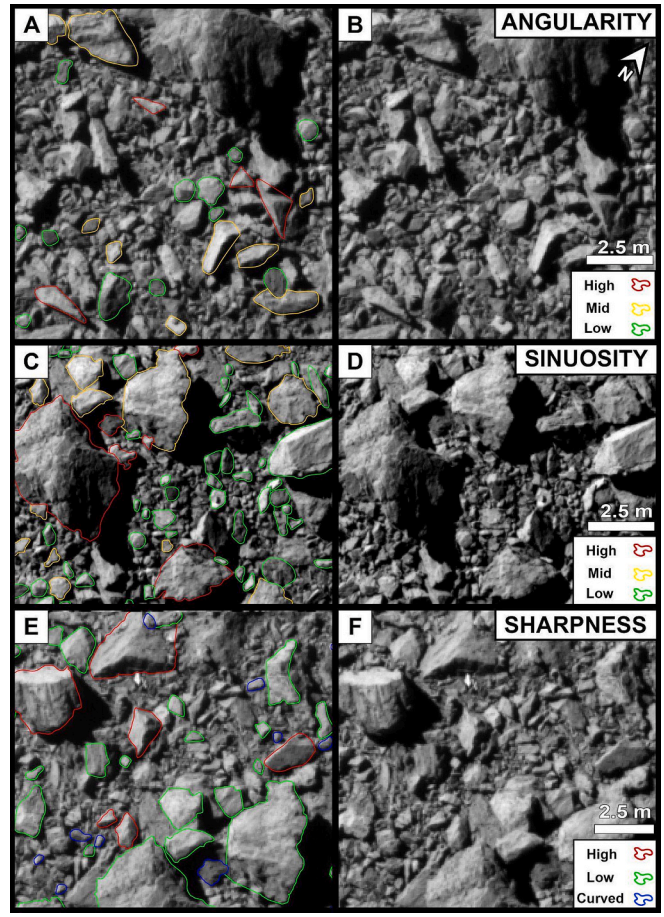

Fig. 2. Examples of boulders classified with the different morphological properties: (A, B) *Angularity,* (C, D) *Sinuosity,* and (E, F) *Sharpness*. On the left, example boulders are indicated through contours. The various colors represent the differences between the various levels (i.e. *low, mid, high, curved*) of each property, as indicated in the legend. On the right, the original image is provided for better understanding. The base image is dart_0401930049_43695_01_iof and the north indicated by the white arrow in panel B stands for the entire picture.

generally result in a macro-scale smoother and uniform surface texture (Kabeya and Legge, 1997). Conversely, coarse-grained rocks (e.g. coarse breccias) tend to have rougher and heterogeneous textures (Kabeya and Legge, 1997). Frequent local sharp gradients in relative brightness indicate a rough surface, while homogeneous tones are associated with smooth surfaces. At this scale *Roughness* appears as an abrupt brightness shift across 3–5 pixels. The boulders' have been divided into *low, medium,* and *high Roughness* categories based on how frequently the relative brightness of their surface changes. The *Low* categories include those boulders whose surface showed extensive homogeneous areas and few changes. Otherwise, the extremely heterogeneous surfaces with a high frequency of variation in the relative brightness and well developed asperities have been categorized as *High.* The *Medium* category gathers all the boulders out from the endmembers. These rocks still show heterogeneity and changes in the surface. Nevertheless, not as much as the *High* category and their asperities are not as well developed as the *High*.

v) *Undulation* property indicates the low-frequency heterogeneity of the rocks' surfaces. Differently from the *Roughness* property, the changes in the relative brightness of the boulders' surfaces are not localized and punctual. Instead, they involve a greater portion of the rock's surface (Fig. 3C, D). The relative brightness change is gradual and at this scale shows a full brightness transition within 7–20 px. We categorized as *High* those boulders whose surface show a clear hummocky surface characterized by low-frequency *Undulation* shapes. Alternatively, we assigned this category also to boulders with presence of distinct clasts embedded in the rock. The clasts appear as localized bumps or corrugation with circular-to-ellipsoidal shape and variable sizes (Fig. 3E, F, G, H). Conversely, we labelled as *low* the boulders which show none of these features and their surface appear as nearly flat.

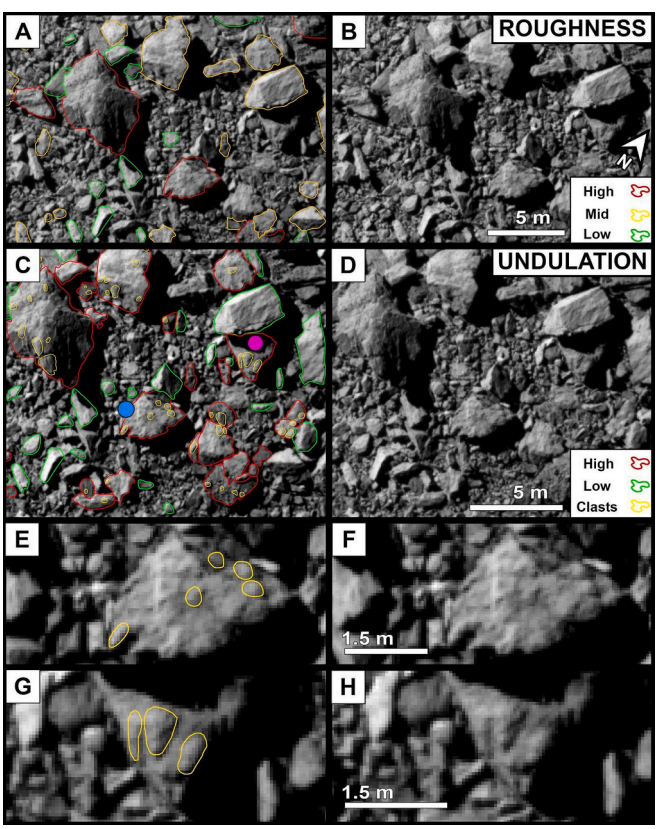

Fig. 3. Examples of boulders classified with the different morphological properties: (A, B) *Roughness,* and (C, D) *Undulation*. Moreover, examples of clasts are shown with closeups of two boulders of the panel C, indicated with a (E, F) blue dot, and a (G, H) pink dot. On the left, example boulders are indicated through contours. The various colors of the panels A and C represent the differences between the various levels (i.e. *low, mid, high, curved*) of each property, as indicated in the legend. On the right, the original image is provided for better understanding. The base image is dart_0401930049_43695_01_iof and the north indicated by the white arrow in panel B stands for the entire picture. (For interpretation of the references to colour in this figure legend, the reader is referred to the web version of this article.)

2.3. Methodology: morphological classes identification

For each mapped boulder, a level was manually assigned to each parameter, provided it was clearly identifiable. To identify the diverse morphological classes we combined the geomorphological observations of the entire area, with specific, distinct, and redundant combinations of *Angularity, Sinuosity, Sharpness, Roughness*, and *Undulation* of the studied boulders. Afterwards, each recognizable boulder was categorized into one of the previously identified morphological classes. To do that, we assigned specific priorities to each property and distinctive features, following a methodology similar to that used in traditional rock classification (Pellant and Pellant, 2021). These criteria are summarized in the flowchart shown in Fig. 4.

Thereafter, we interpreted the properties of these classes with specific lithologies. We have chosen not to use the relative brightness as a discriminating feature because the photometric calibration necessary for an accurate albedo value is not available at such a detailed resolution.

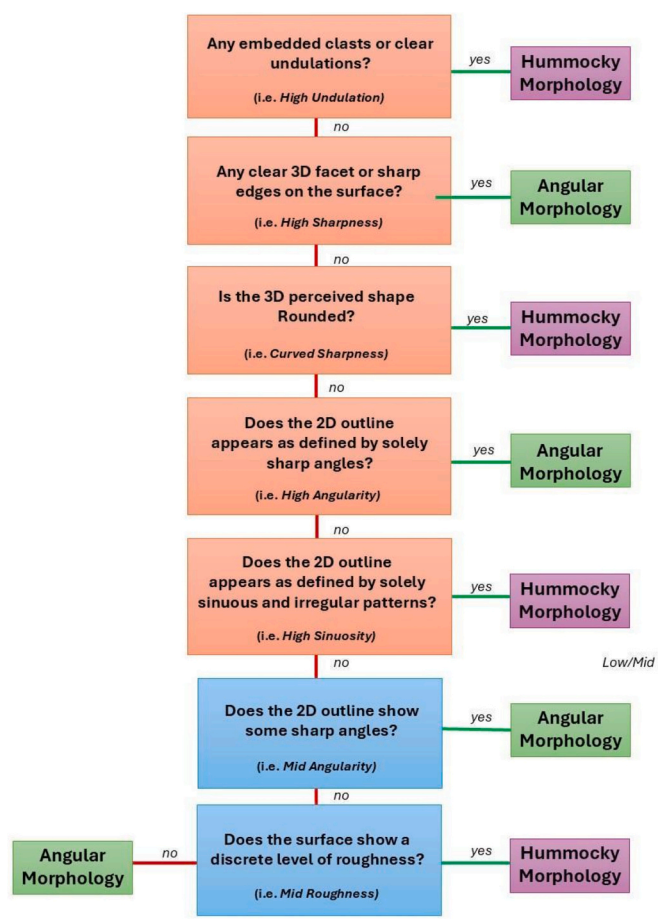

Fig. 4. Flowchart showing the criteria and priorities we adopted in the boulders classification. This is derived from the analysis of the morphological properties conducted on the boulders of the study area. For the definition of *Hummocky* and *Angular* see Section 3.1.

However, we took into account that dissimilar illumination conditions can negatively affect the ability to distinguish these characteristics. Indeed, they can alter the original relative brightness of a lithology and hide or enhance the roughness of a texture, the fracturing, as well as erosional features. Nevertheless, each of the morphological classes we identified comprises hundreds of rocks with random orientation with respect to the illumination direction. We interpreted this natural variability in orientation as a way to approximate different lighting conditions for each class. Since the diverse morphological features remained consistently observable under these varying conditions, we considered this potential observational bias negligible and the morphological classes identification robust.

2.4. Methodology: morphometric analysis

In order to give more consistency to the manual morphological analysis of the boulders, we further investigated the 2D outline shape of the rocks by analyzing several additional nondimensional morphometric parameters (e.g. Blott and Pye, 2008 on this topic). We were not able to analyze morphological properties related to the perceived 3D shape (i.e., *Sharpness*), as this would require a high-resolution Digital Elevation Model (DEM), which is currently unavailable at the scale of this work (Rivkin et al., 2021). Similarly, textural properties such as *Roughness* and *Undulation* could not be quantitatively assessed due to the lack of properly calibrated and photometrically corrected imagery. For this reason, we only considered properties of the outline of the boulders.

Following the methodologies of Cambianica et al. (2019), Robin et al. (2024), and Kohout et al. (2024) we investigated the 2D morphometric parameters *circularity, convexity, sphericity*, *elongation*, *solidity,* and *roundness*. These analyses have been conducted on *Angularity* and *Sinuosity* with the objective of determining if the outline properties we used in our morphological classification as well as their levels (i.e. *high, medium, low*) have any correlation with the main 2D outline parameters (i.e. *circularity, convexity, sphericity*, *elongation*, *solidity,* and *roundness*). Moreover, we also investigated whether any correlation between these parameters and the morphological classes we identified is present. The objective of this additional analysis was to assess the outline's role in defining these classes. For the sake of completeness, we summarized in Table 1 the exact equations we used to compute all these properties. In two dimensions *Sphericity* is defined as the similarity of a boulder's shape to a circle (Riley, 1941). A *sphericity* value equal to 1 indicates that the analyzed shape is a circle with the minimum circumscribing and maximum inscribing rays being the same. *Circularity* (also called compactness) measures how closely the shape resembles a circle of the same area (Cox, 1927; Kohout et al., 2024). Conversely, *solidity* and *convexity* quantify the similarity of the shape to its convex hull, based on area and perimeter, respectively (Mora and Kwan, 2000; Kohout et al., 2024; Cox and Budhu, 2008). If these parameters are equal to 1, it means that the shape of the analyzed boulder corresponds exactly to its convex hull. We assessed boulder's *elongation* by calculating the ratio of length to width in the minimum bounding box of each shape, rotated for optimal fit. Additionally, *roundness* quantifies the acuteness of the corners and edges of the analyzed outline shape (Wadell, 1932, 1933, 1935). This is calculated by comparing the radius at each corner with the radius R of the maximum inscribed circle in the given shape. To compute this value, a set of corners is first identified, and a representative local radius (r) is calculated for each of them. The roundness value is then obtained by averaging the ratios r/R across all corners (Table 1).

Table 1
The morphometric parameters equations computed for each boulder. Their definition follows closely the one used also in Robin et al. (2024), except for Circularity for which we used the perimeter of the convex hull, rather than the perimeter of the polygon to exclude local irregularities.

Morphological Analysis	Equation	Variable Definition	Reference
circularity	$\frac{4\pi A}{P_{CONVEX}{}^2}$	A = projected area; P_{CONVEX} = the perimeter of the convex hull.	Cox, 1927
sphericity	$\frac{R_{INS}}{R_{CIRC}}$	R_{INS}= largest inscribing circle radius; R_{CIRC} = smaller circumscribing circle radius	Riley, 1941
convexity	$\frac{P_{CONVEX}}{P_{POLY}}$	P_{CONVEX} = Perimeter of the convex hull P_{POLY}= Perimeter of the polygon	Cox and Budhu, 2008
solidity	$\frac{A_{POLY}}{A_{CONVEX}}$	A_{CONVEX}= Convex hull area of the boulder	Mora and Kwan, 2000
elongation	$\frac{Bbox\ width}{Bbox\ height}$	$Bbox$= minimum (rotated) fitting bounding box	Blott and Pye, 2008
roundness	$\frac{1}{N}\sum_{i=1}^{N}\frac{r_i}{R_{INS}}$	R_{INS}= the radius of the largest inscribed circle. r_i = the radius of each of the N corners	Wadell, 1932

All these properties were computed using the Python package *"cellseg_gsontools"* (Lehntonen, 2023) with only minor modifications, except for *Roundness* which was computed with a dedicated script. Some of the mapped boulders have shadowed or covered parts that must be interpreted during the mapping process. Therefore, among them, we selected the ones whose interpreted area did not exceed 10 % of their total surface. This has been measured by comparing the extension of the boulders' surfaces with their area covered by the shadows, which were mapped as well. Each hand-traced boulder polygon was then resampled to achieve uniform point spacing along its outline, with each segment measuring exactly one pixel in length. This step was taken to prevent variations in point density (introduced during mapping) from influencing the derived shape properties.

To rigorously quantify the relationships between human-assessed morphological classifications (*Sinuosity, Angularity*, and morphological classes) and algorithmically derived morphometric properties, we applied targeted non-parametric statistical methods. The relationship between the human-defined categories of *Sinuosity* and *Angularity* as well as their levels (i.e. low, medium, and high) and the continuous morphometric parameters (i.e. *circularity, convexity, elongation, roundness, sphericity, and solidity*) was quantified using Kendall's Tau correlation (Kendall, 1938). This approach was chosen to capture the expected monotonic trends in geometric properties as a function of increasing human-assessed *Sinuosity* or *Angularity*. Boxplots were generated to visually represent these distributions and correlations. Furthermore, to statistically compare the distributions of morphometric parameters between the distinct morphologic classes, the Mann-Whitney *U* test was applied (Mann and Whitney, 1947). This non-parametric test is suitable for evaluating differences between two independent groups of continuous data without assuming normality.

3. Results

3.1. Morphological classes and rock categorization

By analyzing the level of categorization (i.e. *high, medium, low, curved*) of the five properties *Angularity, Sinuosity, Sharpness, Roughness,* and *Undulation*, we identified two main morphological classes. One of these groups is represented by boulders showing high levels of *Undulations* and *Sinuosity*, which we called *Hummocky* class. The second group shows rocks characterized by high levels of *Angularity* and *Sharpness* which we called *Angular* class. In addition, we identified two main kinds of fractures, and, as defined by Rüsch and Bickel (2023), one is classified as *near-vertical spalling* while the other as *shear fracture.* The first appears as a fracture parallel to one of the boulder's facets and the second as a curved fracture, which separates the boulders in two smaller

blocks. Nevertheless, these kinds of fractures did not result as a distinctive character between *Hm* and *An* classes, while we found lineations just on two *An* boulders. The boulders of both the morphological classes appear homogeneously distributed among the study area and show no relevant preferential orientation. In Fig. 5 we show eight examples of the two morphological classes.

Angular morphology (An): it is mainly characterized by mid-to-high *Angularity,* high *Sharpness,* low *Sinuosity, Undulation*, and mid-low *Roughness* (Fig. 5 A, C, E). In general, the boulders of this class appear as massive blocks with an overall angular shape both in 2D and perceived 3D. Their texture can have some local irregularities but it is mainly homogeneous and relatively smooth. *Near-vertical spalling* and *shear fracture* (Rüsch and Bickel, 2023) has been observed (Fig. 5 E) and some of the largest *An* boulders show a lineation pattern on their surface (Fig. 5 A, D). The boulder *An3* (Fig. 5E) is one of the most representative boulders of the *An* morphology. Indeed, it shows a regular and consistent 2D outline (i.e. low *Sinuosity*) and a homogenous surface (i.e. low *Undulation*), but characterized by some small irregularities (i.e. mid *Roughness*). Its 3D perceived shape is highly angular, due to at least 3 sharp three-dimensional edges which generate 3 clear facets (i.e. high *Sharpness*).

Hummocky morphology (Hm): it is primarily defined by high *Sinuosity* and *Undulation,* mid-to-high *Roughness*, and low or curve *Sharpness* as well as low *Angularity* (Fig. 5 B, D, E). From a general perspective, the rocks of this morphological class appear weathered with ragged boundaries and flat to curved 3D perceived shape. Moreover, this class is marked by a heterogeneous and hummocky texture due to clear undulation of their surfaces, or to the presence of potential clasts (Fig. 3). The clasts appear as rounded bumps and bulges embedded with the rock, which emerge from their surfaces. The maximum diameter of the identified clasts ranged between ~ 15 cm to ~ 100 cm. As for the Angular morphology class, both *near-vertical spalling* and *shear fracture* (Rüsch and Bickel, 2023) fractures have been observed on the largest rocks. The boulder *Hm2* (Fig. 5D) is one of the most representative boulders of the *Hm* morphology. It shows a 2D outline defined by an irregular pattern and many asperities (i.e. high *Sinuosity*). Its surface is characterized by many high-frequency variations of brightness (i.e. high *Roughness*). Moreover, its 3D perceived shape is generally flat (i.e. low *Sharpness*) but characterized by the presence of embedded clasts (Fig. 3E, F), especially located in the up-right proportion of the boulder, which appear as rounded three-dimensional bulges (i.e. high *Undulation*).

A summary of the criteria we used to discriminate between *Hummocky* and *Angular* morphology is presented in Table 2 and Fig. 4.

In this work we identified 388 boulders larger than 0.4 m in diameter (41 px^2) homogeneously distributed over the full area, for a total of 360.2 m^2 mapped surface. We identified 210 boulders classified as *Hm*, which cover 221.5 m^2 (61.5 %) of the mapped area, while the 178 boulders of the *An* cover 138.7 m^2 (38.5 %) of the studied area. For a better visualization, we produced the lithologic map displayed in Fig. 6. The largest maximum diameter measured among the *An* boulders is 4.03 m, the average is 1.19 m and 275 the median is 0.94 cm. On the other hand, the largest *Hm* boulder's maximum diameter is 6.39 m, the average is 1.09 m and the median is 0.88 cm.

Table 2
summary of the morphological properties considered for both the morphological class.

Morpho. Class	Angularity	Sinuosity	Sharpness	Roughness	Undulation
Hummocky	low	high	low-curved	mid-high	high
Angular	mid-high	low	high	mid-low	low

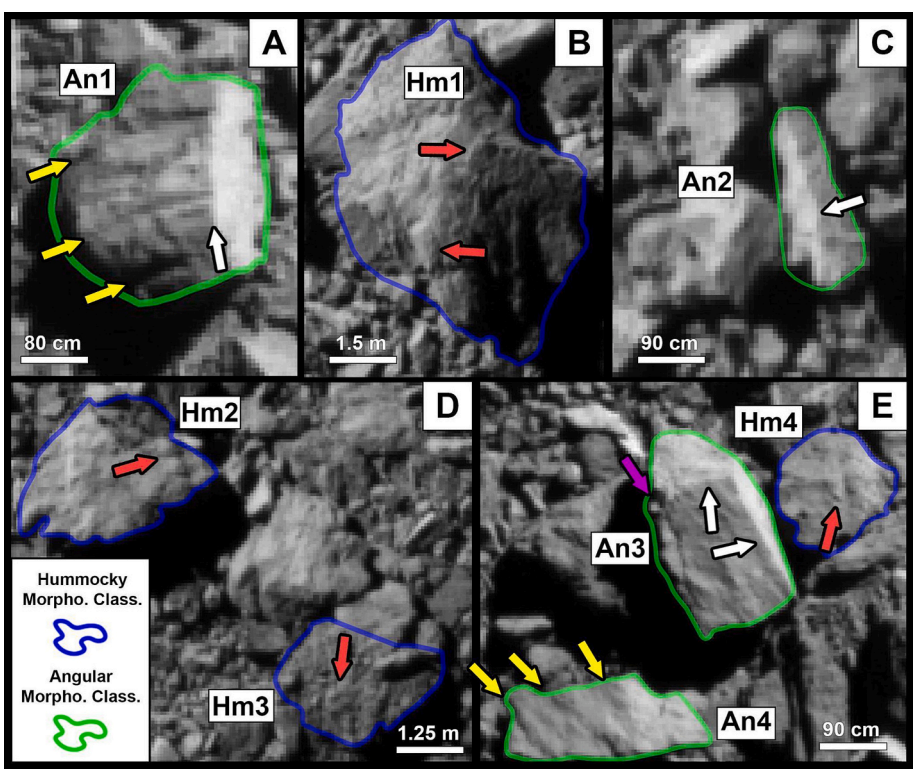

Fig. 5. Examples of the lithologies' endmembers called (A) An1, (B) Hm1, (C) An2, (D) Hm2, Hm3, (E) Hm4, An3, and An4. Arrows indicate the specific and particular properties of the respective lithology like sharp three dimensional edges (white arrows), lineations (yellow arrows), fractures (purple arrow), and bulges (red arrows). (For interpretation of the references to colour in this figure legend, the reader is referred to the web version of this article.)

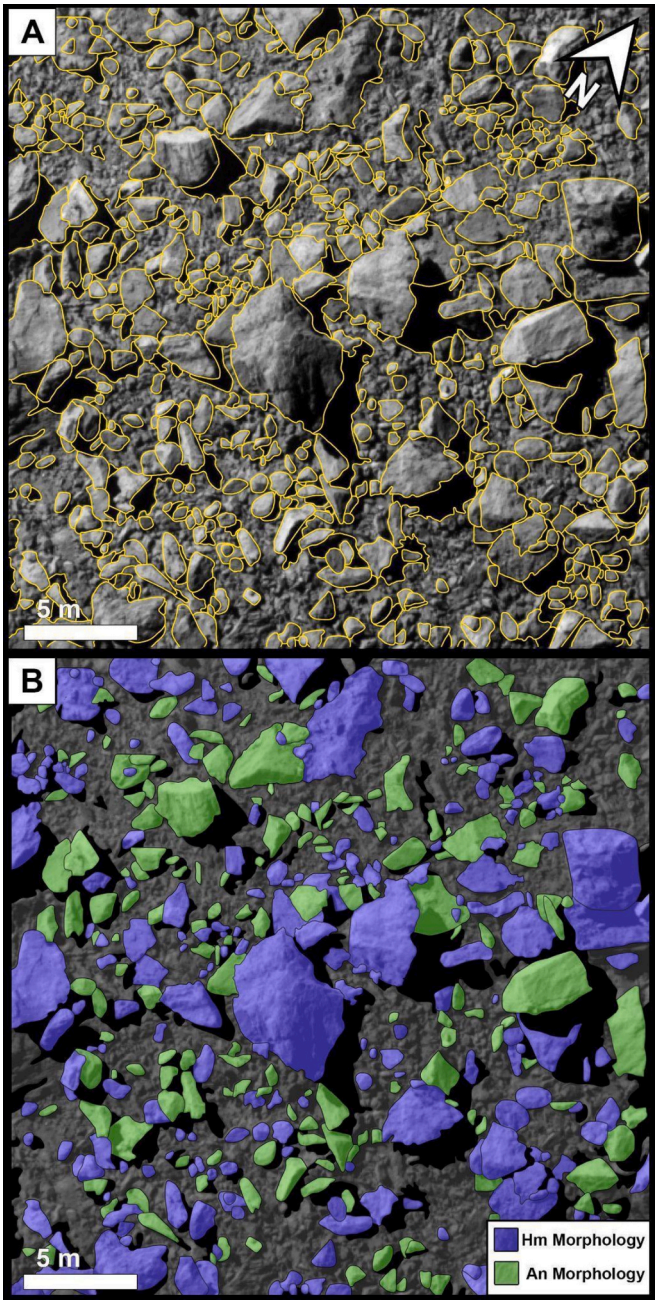

Fig. 6. A) Contours of each mapped and analyzed boulders, manually drawn on the same image as the basemap. North is indicated by the white arrow. B) Map of the Boulder morphologies based on the contacts previously drawn and the morphologies found through the above mentioned properties.

3.2. 2D morphometric parameters

The statistical analyses conducted on *Sinuosity* and *Angularity* (see section 2.4) revealed a statistically significant correlation between their levels (i.e. low, medium, high) and the vast majority of the considered morphometric parameters. The results of this assessment are summarized in Fig. 7 using boxplots, where only the significant correlations are displayed for the sake of clarity.

Sinuosity (Fig. 7) shows a consistent and statistically significant negative monotonic relationship with all examined properties. As *Sinuosity* increases (from categories low to high), measures such as *circularity, convexity, solidity, and roundness* all decrease significantly (all *p*-values < 0.001). Similarly, *Angularity* (Fig. 7) exhibits statistically significant negative monotonic relationships with *circularity, sphericity, elongation*, and *roundness*. On the other hand, *sphericity* and *elongation* did not show significant correlations with *Sinuosity* levels, as *Angularity* with *convexity* and *solidity*.

A similar comparison between distinct *Hm* and *An* boulder classes, conducted using the Mann-Whitney U test (see section 2.4), provides further quantitative validation. While some properties such as convexity and solidity did not show significant differences, others, including circularity, elongation, sphericity, and roundness, exhibited statistically significant differences in their distributions (Fig. 8). These findings underscore that the two classes represent distinct boulder populations with measurable differences in shape.

4. Discussions

4.1. Correlations between the morphometric parameters

Solidity, circularity, and *convexity* values shown in Fig. 7, indicate that the 2D-shape of the boulders with higher *Sinuosity* deviate more from their convex hull shapes, compared to the once with lower *Sinuosity*. We interpreted this result with the boulders with high *Sinuosity* values being correlated with ragged and irregular 2D-boarders, which is consistent with our manual classification. Moreover, the *roundness* values decrease as *Sinuosity* levels increase, suggesting that the number of corners in the outlines of high-*Sinuosity* boulders increases accordingly. However, the different levels of *Sinuosity* do not correlate with *elongation,* and *sphericity*. This can mean that the main 2D-shapes of the boulders are variable in these parameters.

On the other hand, the significant correlations of *Angularity* with *circularity*, *sphericity,* and *elongation* can be interpreted with the outline of the low-*Angularity* boulders being more similar to circles than the high-*Angularity* ones, which instead seems to be more elongated. The inverse proportionality between *Angularity* and *roundness* may suggest that the acuteness of the corner increase together with the *Angularity* property, consistent with its definition. Moreover, the non-correlation between this property and *convexity* and *solidity* underlines that the convex hull is not a significant feature for *Angularity*.

Overall, the results support the idea that the human-assessed morphological categories used in this study are consistent with algorithmically derived geometric properties based on boulder outlines. Although these findings apply only to the geometric properties of boulder outlines, and cannot be directly extended to features related to perceived 3D shape (e.g., *Sharpness*) or texture (e.g., *Roughness* and *Undulation*) they nonetheless support the conclusion that the classifications are systematic and grounded in quantifiable shape characteristics.

The analyses conducted on the *Hm* and *An* morphological classes (shown in Fig. 8) revealed slightly different values between the two, which are consistent with those reported by Robin et al., 2024. These differences are statistically significant as demonstrated by the Mann-Whitney *U* test *p*-values. Specifically, the *Hm* boulders show higher values in *circularity, sphericity*, *elongation*, and *roundness* compared to the *An* ones. This suggests that their outlines are generally more rounded and irregular, as well as less elongated and angular. On the other hand, *solidity* and *convexity* do not show any significant difference. This can be due to similar variability in the convex hull shapes between the two classes. All these differences in morphometric parameters between the two classes support the role of the 2D rock perimeters in defining their morphology. However, the overall small differences observed in some morphometric parameters suggest that an analysis based solely on the 2D outline may be insufficient to fully capture the complexity of boulder morphology. Some characteristics, such as surface texture and the perceived three-dimensional shape, deeply contribute to the morphology of the rocks.

The differences between *Hm* and *An* boulders may be due to a distinct response of the correspondent lithologies to the weathering and erosion processes, which are still active on Dimorphos as micro-impacts and

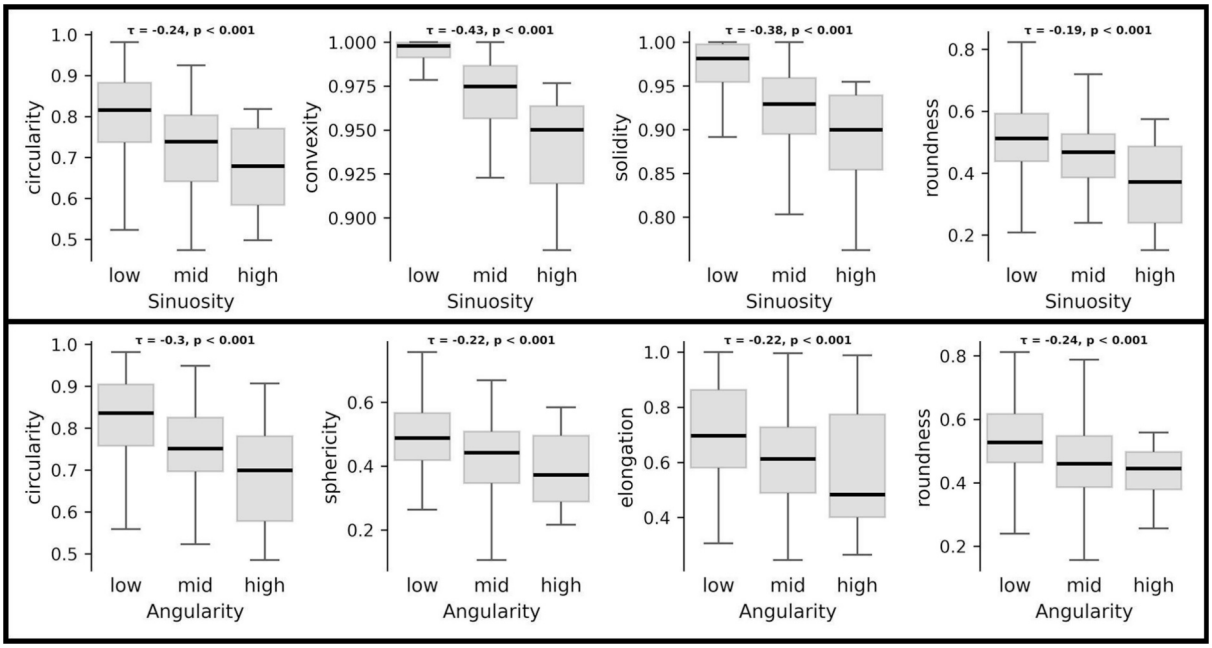

Fig. 7. Geometric morphometric parameters distributions by *Sinuosity* and *Angularity*. Boxplots depict the distributions of various geometric properties across the three levels (low, medium, high) of Angularity (top panels) and Sinuosity (bottom panels). Medians are indicated by black horizontal lines within boxes. Kendall's Tau (τ) correlation coefficients and associated *p*-values, indicating the monotonic relationship between the three levels and the morphometric parameters, are provided above each plot.

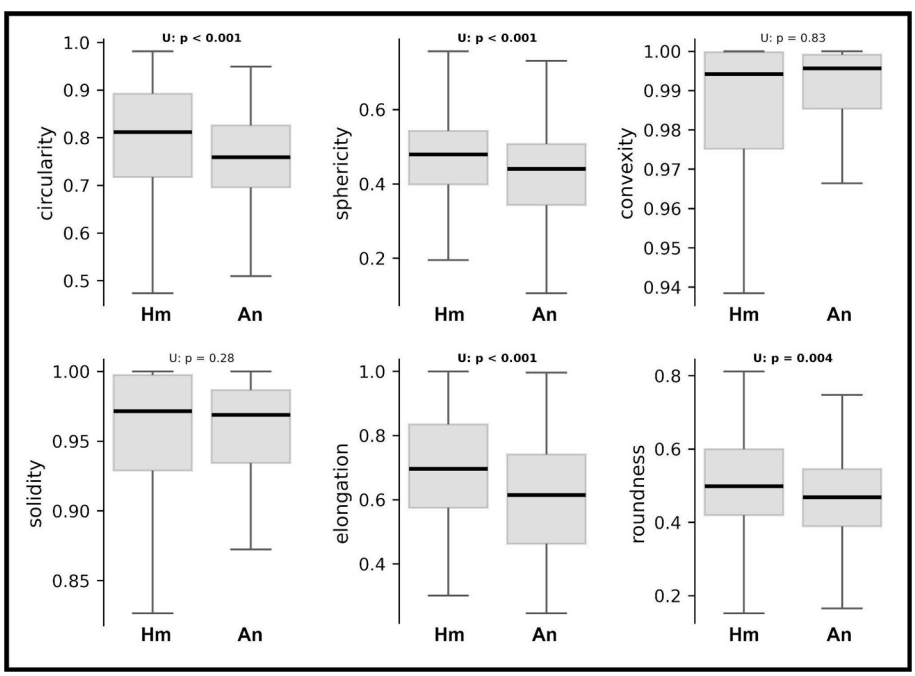

Fig. 8. Boxplots depict the distributions of the considered morphometric parameters (circularity, convexity, elongation, sphericity, solidity, and roundness) for *Hm* and *An* boulders. Unclassified boulders were excluded. Medians are indicated by black horizontal lines within boxes. Annotations above each plot report the Mann-Whitney *U* test *p*-value, indicating the statistical significance of differences in distributions (i.e. interpretable as the significance of the difference in median) between the two classes.

thermal fatigue (Hörz et al., 2020; Barnouin et al., 2024; Lucchetti et al., 2024). Indeed, erosional processes such as meteoritic bombardment and thermal fatigue likely contribute to the eroded, rounded appearance of the *Hm* boulders. These mechanisms would also result in the production of fine-grained particles, which in turn would alter the morphology of the surface by infilling surface cavities forming smooth "ponded" features (Cheng et al., 2002; Fujiwara et al., 2006; Buratti et al., 2024). All these processes likely equally involved all the boulders present within the study area (Lucchetti et al., 2024). Nevertheless, different mineralogical composition, grain sizes and mechanical properties of the rocks (such as cohesion), can significantly influence the effects of these weathering processes. In particular, more cohesive rocks are more resistant to weathering than friable or poorly-consolidated lithologies (Neukum et al., 1973; Hörz et al., 2020). These differences in erosions

lead, in turn, to differences in morphologies such as *Hm* and *An*. Therefore, these results indicate that the lithologies associated with *Hm* rocks seems to be more affected by the weathering processes with respect to the *A* one.

4.2. Lithology interpretation

The various morphological features of rocks, such as their fracture and erosion patterns, or specific textural characteristics like the presence of clasts or lineations, can be correlated with specific mineralogical properties (Colman, 1981; Panizza, 1996; Kabeya and Legge, 1997; Carroll, 2012; Panizza and Goudie, 2013). Therefore, since the *Hummocky* and *Angular* morphological classes show different characteristics, we interpreted them with distinct potential lithologies. Moreover, at this image resolution, we did not find any boulder which seems to be composed of multiple lithologies.

Hm class is mainly characterized by boulders showing ragged boundaries and undulated surfaces, with both *near-vertical spalling* and *shear fractures* that are likely linked with thermal fatigue processes active on Dimorphos surface (Lucchetti et al., 2024). These traits can indicate more friable rocks prone to weathering and erosion processes, which suggest a lithology with a low cohesion. These characteristics combined with the presence of clasts, make them consistently similar to poorly consolidated breccias, characterized by more cohesive clasts bounded by a finer matrix. Similar characteristics have been already observed on the S-type (25143) Itokawa by Noguchi et al. (2010), on the C-type Ryugu (Sugimoto et al., 2021), and the B-type Bennu (Jawin et al., 2023). Although the different classes of these asteroids, in all these cases, rounded rocks with bumps and protrusions were defined as breccias (Fig. 9). Moreover, such boulders also show ragged outlines and

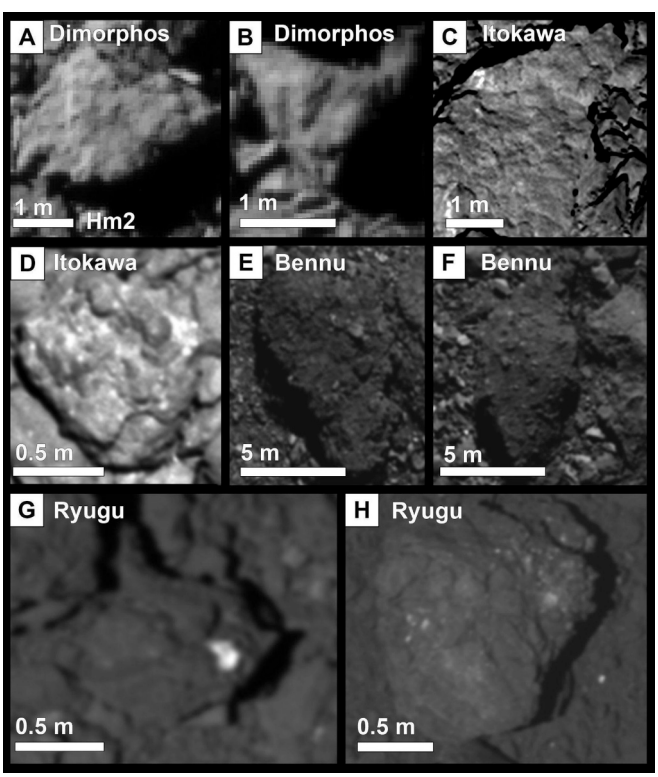

Fig. 9. Comparison between the breccias found on (A, B) Dimorphos (boulder Hm2 shown in Fig. 3) by our results and (C, D) Itokawa, (E, F) Bennu, and (G, H) Ryugu. Although Bennu and Ryugu are classified as B-type and C-type respectively, the shape and the hummocky texture of all the shown breccias are very similar. Itokawa's images with comparable spatial scale adapted from Noguchi et al. (2010) and Ryugu's images adapted from (Sugimoto et al., 2021).

a weathered or eroded surface like it has been observed on Dimorphos. The genesis of these kinds of rocks is extremely variable and can be summarized by three different groups of geological processes, i.e. sedimentary, like ejecta deposition and compaction (Merstallinger et al., 2009; Spray, 2016), impacts (Bischoff et al., 2006; Beitz et al., 2016), and igneous if the parent body had reached an advanced state of differentiation (Ollier, 2007; Shukla and Sharma, 2018). The most probable kinds of breccias we expect to find on Dimorphos are the sedimentary and impact ones (Ollier, 2007; Merstallinger et al., 2009; Spray, 2016) because they are the most common processes occurring on planetesimals. However, if the parent body had reached an advanced state of differentiation before the catastrophic event, igneous and igneous-hydrothermal could also be present (Tamas and Milési, 2003; Ollier, 2007; Cas et al., 2011). In any case, all the above-mentioned processes responsible for forming breccias primarily affect the upper hundreds of meters of the planetesimal's crust (Ollier, 2007; Bischoff et al., 2006; Beitz et al., 2016; Spray, 2016; Shukla and Sharma, 2018). Thus, even though these mechanisms differ significantly, any kind of breccias on Didymos or Dimorphos are related to the shallowest portion of their original parent body.

On the other hand, *An* class shows boulders characterized by sharp three-dimensional edges, planar facets, and a relatively homogeneous and smoother surface with respect to *Hm* rocks. The lineation patterns observed on some of the largest *An* boulders may have formed as a result of the impact process (Baratoux and Reimold, 2016) directly on Dimorphos' surface. These characteristics suggest a lithology with high internal cohesion, a relatively fine grain size (Grieve, 2005) and less prone to the weathering processes (McSween Jr, 1989; Britt and Consolmagno, 2003; Consolmagno et al., 2008; Pohl and Britt, 2020). In the planetesimal environment, multiple processes are capable of generating rock with such properties. These rocks can be interpreted as *achondritic/intrusive* igneous rocks. Their presence would imply a parent body at least partly-differentiated and their amount would increase with the planetesimal degree of differentiation (Weiss and Elkins-Tanton, 2013; Ostrowski and Bryson, 2019). *Effusive* igneous rocks may also be present and are typical of more superficial portions of the parent body and would likely appear as similarly cohesive rocks. However, the processes driving their genesis, like impact melts and effusive eruptions, are typically confined in localized areas and produce only relatively small volumes of such material compared to the entire body. Therefore, it is improbable that the *An* morphology is representative of effusive lithologies. Indeed, our results revealed that *An* rocks cover a total of 38.5 % of the studied area. The formation and evolution of Dimorphos were likely chaotic and characterized by multiple collisions and mass shedding (Agrusa et al., 2024; Pajola et al., 2024; Raducan et al., 2024). Based on this, we assume that the fragments of the parent body now composing Dimorphos are nearly homogeneously mixed. Consequently, such a high abundance of *An* rocks appears inconsistent with an effusive origin. Another possible interpretation of the *An* rocks is considering them as.

highly-metamorphosed chondritic material, which at our scale of observation show characteristics similar to the achondrites. However, both the achondritic and highly-metamorphosed chondritic lithologies are thought to come from a deeper part of the parent body with respect to the breccias (Turner, 1948; Weiss and Elkins-Tanton, 2013; Shukla and Sharma, 2018). Finally, *An* boulders can also be interpreted as ultra-lithified sedimentary rocks. These rocks have high cohesive properties and, at our scale of observation, may resemble igneous or metamorphic rocks. However, we did not notice any embedded clasts within this morphological class. Therefore, either these rocks do not have any clasts, or they are smaller than the resolution of our observations. Nonetheless, the degree of apparent cohesion supports the hypothesis that the *An* rocks originated from a different and deeper region of the parent body compared to *Hm* ones.

However, the pixel scale of our data limits our investigation up to cm-scale. As a result, we were unable to distinguish rock types with

greater accuracy. Additionally, the presence of further lithologies cannot be excluded. Such analysis will be extended thanks to the ESA/Hera that was successfully launched on 7th October 2024 to investigate the Didymos and Dimorphos' surfaces (Michel et al., 2022). The Hera spacecraft will arrive to (65803) Didymos system at the end of 2026, and will deeply study it thanks to the Asteroid Framing Cameras (AFC, Küppers and Fernandez, 2021; Michel et al., 2022), a visible spectral imager (Hyperscout-H; Popescu et al., 2024), the Asteroid thermal imager (TIRI; Michel et al., 2022; Henry et al., 2024), and a lidar (PALT; Michel et al., 2022; Dias et al., 2022). This payload will let Hera observe the (65803) Didymos system with much higher spatial and spectral resolution than the DART mission did. In particular the ASPECT spectrometers in the near IR and the TIRI thermal imager will help identify possible compositional differences. Additionally, the Hera spacecraft will be also equipped with two cubesats Juventas (Goldberg et al., 2019; Michel et al., 2022) and Milani (Michel et al., 2022; Pugliatti et al., 2022). These cubesats will be released close to the target at 10–20 km from Didymos-Dimorphos. Together with the Hera spacecraft they will perform several very close flybys of Dimorphos (pericenter distance <2 km) and, after the first phase of the mission, Milani will try to land on Didymos, while Juventas on Dimorphos (Küppers and Fernandez, 2021; Michel et al., 2022).

Such data will be pivotal to analyze the surface of the binary asteroid in greater detail and refine our lithological classification on both asteroids' boulders and cobbles. In particular, they will allow us to:

i) determine whether the lithological mixing observed at the DART impact site is representative of the entire surface of Dimorphos; ii) verify the presence of smaller clasts embedded within the rocks, exploiting the high spatial resolution of AFC; iii) identify potential differences in composition between the two lithological classes; iv) further investigate the cohesion of the lithologies through the TIRI's thermal models in combination with the fractures analysis conducted with the AFC data; v) analyze differences in rock morphology and spatial distribution between Didymos and Dimorphos; and vi) examine the morphological changes induced by the DART impact on the targeted rocks and the possible exposure of deeper, previously unobserved lithologies.

5. Conclusions

In this work we studied the morphologies of the boulders and cobbles present on Dimorphos' surface using the image acquired by DRACO camera with a pixel scale of 5.5 cm pixel^{-1}. Such resolution allowed us to deeply observe both the 2D outline and perceived 3D shapes of the rocks, as well as their texture and weathering appearance. We selected five discriminating morphological properties (i.e. *Angularity, Sinuosity, Sharpness, Roughness, and Undulation*) and based on them we identified two distinct morphological classes. The *An* one is mainly defined by its angular and straight outline shape with sharp three-dimensional edges which form well-defined sub-planar facets. Moreover, the rocks of this class show low-to-mid *Roughness* and the presence of lineations on some boulders. On the other hand, the *Hm* morphology is characterized by ragged and irregular 2D perimeters, a flat-to-curve 3D perceived shape and a rough and hummocky texture due to the presence of clasts on its surface.

We also found a statistically significant separation of *circularity, sphericity, elongation* and *roundness* (Cambianica et al., 2019; Robin et al., 2024; Kohout et al., 2024), as confirmed by the *p*-value found through the Mann-Whitney *U* test. These outcomes indicate that the 2D outlines of *Hm* boulders are more rounded and irregular, and less angular and elongated compared to those of the *An* class.

We produced a map identifying the morphology of each boulder larger than 0.4 m in the study area. 210 boulders were recognized as *Hm* and cover 221.5 m^2, which represents 61.5 % of the total mapped area (Fig. 4). At the same time, 178 boulders were identified as *An*, which covers 138.7 m^2, i.e. 38.5 % of the mapped area (Fig. 6). Due to their respective similar morphological characteristics, we interpreted the *Hm* boulders as poorly consolidated breccias, while the *An* morphology as an achondritic or highly-metamorphosed chondritic lithology. The first lithology is typical of the most superficial part of the planetesimal's crust (Shukla and Sharma, 2018), and indicates a surface involved in many brecciation processes, especially the sedimentary (ejecta emplacement and compaction) and impact activities (Bischoff et al., 2006; Merstallinger et al., 2009; Spray, 2016). Conversely, the lithologies associated with *An* boulders should come from deeper regions of the planetesimal (Shukla and Sharma, 2018).

This work marks a first step toward unraveling the lithologic complexity of Dimorphos. However, we analyzed just a small region compared to its whole surface. Additionally, we could not analyze smaller portions of the boulders due to the pixel scale of 5.5 cm/px and no spectral resolution which prevent us from discriminating among small clasts, fine textures, and recognizing different minerals. Therefore, many questions are still open but will be likely solved with the upcoming Hera mission's high resolution data. Hera's contribution to the study of Didymos and Dimorphos lithology will come through observing the entire Dydimos and Dimorphos' surfaces with different instruments of the scientific payload and with different illumination conditions. Thanks to Hera data this work will be greatly improved, erasing bias like illumination conditions, and leading to a more accurate study of the boulders and cobbles' composition and morphological characteristics.

CRediT authorship contribution statement

F. Tusberti: Writing – review & editing, Writing – original draft, Visualization, Validation, Methodology, Investigation, Formal analysis, Conceptualization. **M. Pajola:** Writing – review & editing, Writing – original draft, Validation, Methodology, Investigation, Funding acquisition, Formal analysis, Conceptualization. **L. Penasa:** Writing – review & editing, Writing – original draft, Methodology, Investigation, Formal analysis. **A. Lucchetti:** Writing – review & editing, Writing – original draft, Methodology, Investigation. **M. Massironi:** Writing – review & editing, Validation, Methodology, Investigation, Conceptualization. **G. Munaretto:** Writing – review & editing. **J. Beccarelli:** Writing – review & editing. **R. Pozzobon:** Writing – review & editing. **C. Rossi:** Writing – review & editing. **G. Poggiali:** Writing – review & editing. **N. Murdoch:** Writing – review & editing. **C.Q. Robin:** Writing – review & editing. **A. Duchene:** Writing – review & editing. **M. Amoroso:** Writing – review & editing. **I. Bertini:** Writing – review & editing. **J.R. Brucato:** Writing – review & editing. **A. Capannolo:** Writing – review & editing. **S. Caporali:** Writing – review & editing. **M. Ceresoli:** Writing – review & editing. **G. Cremonese:** Writing – review & editing. **M. Dall'Ora:** Writing – review & editing. **V. Della Corte:** Writing – review & editing. **J.D.P. Deshapriya:** Writing – review & editing. **E. Dotto:** Writing – review & editing. **E. Mazzotta Epifani:** Writing – review & editing. **I. Gai:** Writing – review & editing. **E. Gramigna:** Writing – review & editing. **P.H.A. Hasselmann:** Writing – review & editing. **S. Ieva:** Writing – review & editing. **G. Impresario:** Writing – review & editing. **S. Ivanovski:** Writing – review & editing. **R. Lasagni Manghi:** Writing – review & editing. **M. Lavagna:** Writing – review & editing. **M. Lombardo:** Writing – review & editing. **D. Modenini:** Writing – review & editing. **P. Palumbo:** Writing – review & editing. **D. Perna:** Writing – review & editing. **S. Pirrotta:** Writing – review & editing. **A. Rossi:** Writing – review & editing. **P. Tortora:** Writing – review & editing. **M. Zannoni:** Writing – review & editing. **G. Zanotti:** Writing – review & editing. **A. Zinzi:** Writing – review & editing. **B. Buratti:** Writing – review & editing. **J.M. Trigo-Rodrigez:** Writing – review & editing. **L. Gomez Casajus:** Writing – review & editing.

Declaration of competing interest

The authors declare that they have no known competing financial interests or personal relationships that could have appeared to influence the work reported in this paper.

Acknowledgements

We extend our sincere gratitude to Ottaviano Rüsch and an anonymous Reviewer for their valuable comments and suggestions, which significantly improved this work. This work was supported by the Italian Space Agency (ASI) within the LICIACube project (ASI-INAF agreement n. 2019-31-HH.0) and Hera project (ASI-INAF agreement n. 2022-8-HH.0). Matteo Massironi and Riccardo Pozzobon have been supported by EPN 2024-RI under grant agreement N. 871149. JMT-R acknowledges financial support from the Spanish project PID2021-128062NB-I00 funded by MCIN/AEI/10.13039/501100011033.

Data availability

Data will be made available on request.

References

Agrusa, H.F., Zhang, Y., Richardson, D.C., Pravec, P., Ćuk, M., Michel, P., et al., 2024. Direct N-body simulations of satellite formation around small asteroids: Insights from DART'S encounter with the Didymos system. Planet. Sci. J. 5 (2), 54. https://doi.org/10.3847/PSJ/ad206b.

Baratoux, D., Reimold, W.U., 2016. The current state of knowledge about shatter cones: introduction to the special issue. Meteorit. Planet. Sci. 51 (8), 1389–1434. https://doi.org/10.1111/maps.12678.

Barnouin, O., Ballouz, R.L., Marchi, S., Vincent, J.B., Agrusa, H., Zhang, Y., et al., 2024. The Geology and Evolution of a the Near-Earth Binary Asteroid System (65803) Didymos.

Beitz, E., Blum, J., Parisi, M.G., Trigo-Rodríguez, J.M., 2016. The collisional evolution of undifferentiated asteroids and the formation of chondritic meteoroids. Astrophys. J. 824 (12). https://doi.org/10.3847/0004-637X/824/1/12, 29 pp.

Bigot, J., Lombardo, P., Murdoch, N., Scheeres, D.J., Vivet, D., Zhang, Y., et al., 2024. The bearing capacity of asteroid (65803) Didymos estimated from boulder tracks. Nat. Commun. 15 (1), 6204.

Bischoff, A., Scott, E.R., Metzler, K., Goodrich, C.A., 2006. Nature and origins of meteoritic breccias. In: Meteorites and the Early Solar System II, pp. 679–712.

Blott, S.J., Pye, K., 2008. Particle shape: a review and new methods of characterization and classification. Sedimentology 55 (1), 31–63. https://doi.org/10.1111/j.1365-3091.2007.00892.x.

Britt, D.T., Consolmagno, G.J.S.J., 2003. Stony meteorite porosities and densities: a review of the data through 2001. Meteorit. Planet. Sci. 38 (8), 1161–1180. https://doi.org/10.1111/j.1945-5100.2003.tb00305.x.

Buratti, B.J., Pittichová, J., Mishra, I., Hillier, J.K., Mosher, J.A., Chesley, S.R., et al., 2024. Pre-impact albedo map and photometric properties of the (65803) Didymos asteroid binary system from DART and ground-based data. Planet. Sci. J. 5 (3), 83. https://iopscience.iop.org/article/10.3847/PSJ/ad2b60.

Cambianica, P., Cremonese, G., Naletto, G., Lucchetti, A., Pajola, M., Penasa, L., et al., 2019. Quantitative analysis of isolated boulder fields on comet 67P/Churyumov-Gerasimenko. Astron. Astrophys. 630, A15.

Carroll, D., 2012. Rock Weathering. Springer Science & Business Media.

Cas, R., Giordano, G., Balsamo, F., Esposito, A., Mastro, S.L., 2011. Hydrothermal breccia textures and processes: Lisca bianca islet, Panarea volcano, Aeolian Islands, Italy. Econ. Geol. 106 (3), 437–450. https://doi.org/10.2113/econgeo.106.3.437.

Chabot, N.L., Rivkin, A.S., Cheng, A.F., Barnouin, O.S., Fahnestock, E.G., Richardson, D. C., et al., 2024. Achievement of the planetary defense investigations of the double asteroid redirection test (DART) mission. Planet. Sci. J. 5 (2), 49. https://doi.org/10.3847/PSJ/ad16e6.

Cheng, A.F., Izenberg, N., Chapman, C.R., Zuber, M.T., 2002. Ponded deposits on asteroid 433 Eros. Meteorit. Planet. Sci. 37 (8), 1095–1105. https://onlinelibrary.wiley.com/doi/10.1111/j.1945-5100.2002.tb00880.x.

Colman, S.M., 1981. Rock-weathering rates as functions of time. Quat. Res. 15 (3), 250–264. https://doi.org/10.1016/0033-5894(81)90029-6.

Consolmagno, G.J., Britt, D.T., Macke, R.J., 2008. The significance of meteorite density and porosity. Geochemistry 68 (1), 1–29. https://doi.org/10.1016/j.chemer.2008.01.003.

Cox, E.P., 1927. A method of assigning numerical and percentage values to the degree of roundness of sand grains. J. Paleontol. 1 (3), 179–183. http://www.jstor.org/stable/1298056.

Cox, M.R., Budhu, M., 2008. A practical approach to grain shape quantification. Eng. Geol. 96 (1–2), 1–16. https://doi.org/10.1016/j.enggeo.2007.05.005.

Daly, R.T., Ernst, C.M., Barnouin, O.S., Chabot, N.L., Rivkin, A.S., Cheng, A.F., et al., 2023. Successful kinetic impact into an asteroid for planetary defence. Nature 616 (7957), 443–447. https://doi.org/10.1038/s41586-023-05810-5.

De León, J., Licandro, J., Duffard, R., Serra-Ricart, M., 2006. Spectral analysis and mineralogical characterization of 11 olivine–pyroxene rich NEAs. Adv. Space Res. 37 (1), 178–183.

Deshapriya, J.D.P., Hasselmann, P.H., Gai, I., Hirabayashi, M., Dotto, E., Rossi, A., et al., 2023. Characterization of the DART impact ejecta plume on Dimorphos from LICIACube observations. Planet. Sci. J. 4 (12), 231. https://doi.org/10.3847/PSJ/ad09ba.

Dias, N.G., Gordo, P., Onderwater, H., Melicio, R., Amorim, A., 2022. Analysis on the isostatic bipod mounts for the HERA mission LIDAR. Appl. Sci. 12 (7), 3497. https://doi.org/10.3390/app12073497.

Dotto, E., Della Corte, V., Amoroso, M., Bertini, I., Brucato, J.R., Capannolo, A., et al., 2021. LICIACube-the light Italian Cubesat for imaging of asteroids in support of the NASA DART mission towards asteroid (65803) Didymos. Planet. Space Sci. 199, 105185. https://doi.org/10.1016/j.pss.2021.105185.

Dotto, E., Deshapriya, J.D.P., Gai, I., Hasselmann, P.H., Mazzotta Epifani, E., Poggiali, G., et al., 2024. The Dimorphos ejecta plume properties revealed by LICIACube. Nature 627 (8004), 505–509. https://doi.org/10.1038/s41586-023-06998-2.

Fletcher, Z.J., Ryan, K.J., Maas, B.J., Dickman, J.R., Hammond, R.P., Bekker, D.L., et al., 2018, July. Design of the Didymos Reconnaissance and Asteroid Camera for OpNav (DRACO) on the double asteroid redirection test (DART). In: Space Telescopes and Instrumentation 2018: Optical, Infrared, and Millimeter Wave, vol. 10698. SPIE, pp. 602–612. https://doi.org/10.1117/12.2310136.

Fujiwara, A., Kawaguchi, J., Yeomans, D.K., Abe, M., Mukai, T., Okada, T., et al., 2006. The rubble-pile asteroid Itokawa as observed by Hayabusa. Science 312 (5778), 1330–1334.

Goldberg, H.R., Karatekin, Ö., Ritter, B., Herique, A., Tortora, P., Prioroc, C., et al., 2019. The Juventas CubeSat in Support of ESA'S Hera Mission to the Asteroid Didymos.

Grieve, R.A.F., 2005. Impact structures. In: Of Selley, Richard, C., McCocks, L. Robin, Plimer, Ian R. (Eds.), Encyclopedia of Geology, vol. 5. Elsevier Limited, Oxford. https://doi.org/10.1016/B0-12-369396-9/00130-1.

Henry, G., Karatekin, Ã., Berk Senel, C., 2024. Thermal infrared imager (TIRI) simulation with Kalast for Hera flyby targets. In: Europlanet Science Congress 2024. https://doi.org/10.5194/epsc2024-1167 (pp. EPSC2024-1167).

Hirata, N., Barnouin-Jha, O.S., Honda, C., Nakamura, R., Miyamoto, H., Sasaki, S., et al., 2009. A survey of possible impact structures on 25143 Itokawa. Icarus 200 (2), 486–502.

Hörz, F., Basilevsky, A.T., Head, J.W., Cintala, M.J., 2020. Erosion of lunar surface rocks by impact processes: a synthesis. Planet. Space Sci. 194, 105105. https://doi.org/10.1016/j.pss.2020.105105.

Ieva, S., Epifani, E.M., Perna, D., Dall'Ora, M., Petropoulou, V., Deshapriya, J.D.P., et al., 2022. Spectral rotational characterization of the Didymos system prior to the DART impact. Planet. Sci. J. 3 (8), 183.

Jaumann, R., Schmitz, N., Ho, T.M., Schröder, S.E., Otto, K.A., Stephan, K., Kouyama, T., 2019. Images from the surface of asteroid Ryugu show rocks similar to carbonaceous chondrite meteorites. Science 365 (6455), 817–820. https://doi.org/10.3390/app12073497.

Jawin, E.R., Ballouz, R.L., Ryan, A.J., Kaplan, H.H., McCoy, T.J., Al Asad, M.M., et al., 2023. Boulder diversity in the nightingale region of asteroid (101955) Bennu and predictions for physical properties of the OSIRIS-REx sample. J. Geophys. Res. Planets 128 (12), e2023JE008019.

Jin, Z., Bose, M., 2019. New clues to ancient water on Itokawa. Sci. Adv. 5 (5), eaav8106.

Kabeya, K.K., Legge, T.F.H., 1997. Relationship between grain size and some surface roughness parameters of rock joints. Int. J. Rock Mech. Min. Sci. 34 (3–4), 146–e1. https://doi.org/10.1016/S1365-1609(97)00186-X.

Kendall, M.G., 1938. A new measure of rank correlation. Biometrika 30 (1–2), 81–93. https://doi.org/10.1093/biomet/30.1-2.81.

Kohout, T., Pajola, M., Soini, A.J., Lucchetti, A., Luttinen, A., Duchêne, A., et al., 2024. Impact disruption of Bjurböle porous chondritic projectile. Planet. Sci. J. 5 (5), 128. https://doi.org/10.3847/PSJ/ad4266.

Küppers, M., Fernandez, J.G., 2021. Hera mission requirements document 2.10. ESA-TECSH-RS-022793.

Lauretta, D.S., Bartels, A.E., Barucci, M.A., Bierhaus, E.B., Binzel, R.P., Bottke, W.F., et al., 2015. The OSIRIS-REx target asteroid (101955) Bennu: constraints on its physical, geological, and dynamical nature from astronomical observations. Meteorit. Planet. Sci. 50 (4), 834–849.

Lauretta, D.S., Balram-Knutson, S.S., Beshore, E., Boynton, W.V., Drouet d'Aubigny, C., DellaGiustina, D.N., et al., 2017. OSIRIS-REx: sample return from asteroid (101955) Bennu. Space Sci. Rev. 212, 925–984.

Lauretta, D.S., DellaGiustina, D.N., Bennett, C.A., Golish, D.R., Becker, K.J., Balram-Knutson, S.S., et al., 2019. The unexpected surface of asteroid (101955) Bennu. Nature 568 (7750), 55–60.

Lehntonen, O., 2023. Tools for features extraction in cell and tissue segmentation maps. https://zenodo.org/doi/10.5281/zenodo.10617987.

Lucchetti, A., Cambioni, S., Nakano, R., Barnouin, O.S., Pajola, M., Penasa, L., et al., 2024. Fast boulder fracturing by thermal fatigue detected on stony asteroids. Nat. Commun. 15 (1), 6206.

Mann, H.B., Whitney, D.R., 1947. On a test of whether one of two random variables is stochastically larger than the other. Ann. Math. Stat. 50–60.

McSween Jr., H.Y., 1989. Achondrites and igneous processes on asteroids. In: Annual Review of Earth and Planetary Sciences, vol. 17. Annual Reviews, Inc, Palo Alto, CA, pp. 119–140 (A89-51245 22-46).

Merstallinger, A., Sales, M., Semerad, E., Dunn, B.D., 2009. Assessment of cold welding between separable contact surfaces due to impact and fretting under vacuum, vol. 279. ESA Communication Production Office, p. 57.

Michel, P., Küppers, M., Bagatin, A.C., Carry, B., Charnoz, S., De Leon, J., et al., 2022. The ESA Hera mission: detailed characterization of the DART impact outcome and of the binary asteroid (65803) Didymos. Planet. Sci. J. 3 (7), 160.

Mora, C.F., Kwan, A.K.H., 2000. Sphericity, shape factor, and convexity measurement of coarse aggregate for concrete using digital image processing. Cem. Concr. Res. 30 (3), 351–358. https://doi.org/10.1016/S0008-8846(99)00259-8.

Naidu, S.P., Chesley, S.R., Moskovitz, N., Thomas, C., Meyer, A.J., Pravec, P., et al., 2024. Orbital and physical characterization of asteroid Dimorphos following the DART impact. Planet. Sci. J. 5 (3), 74. https://doi.org/10.3847/PSJ/ad26e7.

Neukum, G., Hörz, F., Morrison, D.A., Hartung, J.B., 1973. Crater populations on lunar rocks. Proc. Lunar Sci. Conf. 4, 3255.
Noguchi, T., Tsuchiyama, A., Hirata, N., Demura, H., Nakamura, R., Miyamoto, H., Zolensky, M.E., 2010. Surface morphological features of boulders on asteroid 25143 Itokawa. Icarus 206 (1), 319–326. https://doi.org/10.1016/j.icarus.2009.09.002.
Ollier, C.D., 2007. Breccia-filled pipes: distinguishing between volcanic and non-volcanic origins. Geogr. Fis. Din. Quat. 30 (1), 63–76.
Ostrowski, D., Bryson, K., 2019. The physical properties of meteorites. Planet. Space Sci. 165, 148–178. https://doi.org/10.1016/j.pss.2018.11.003.
Pajola, M., Barnouin, O.S., Lucchetti, A., Hirabayashi, M., Ballouz, R.L., Asphaug, E., et al., 2022. Anticipated geological assessment of the (65803) didymos–dimorphos system, target of the DART–LICIACube mission. Planet. Sci. J. 3 (9), 210.
Pajola, M., Tusberti, F., Lucchetti, A., Barnouin, O., Cambioni, S., Ernst, C.M., et al., 2024. Evidence for multi-fragmentation and mass shedding of boulders on rubble-pile binary asteroid system (65803) Didymos. Nat. Commun. 15 (1), 6205.
Panizza, M., 1996. Environmental Geomorphology. Elsevier.
Panizza, M., Goudie, A., 2013. Encyclopedia of. Geomorphology. https://doi.org/10.4324/9780203381137.
Pellant, C., Pellant, H., 2021. Rocks and Minerals. Dorling Kindersley Ltd.
Penasa, L., Frigeri, A., Pozzobon, R., Brandt, C.H., De Toffoli, B., Naß, A., Rossi, A.P., Massironi, M., 2020. Constructing and deconstructing geological maps: a QGIS plugin for creating topologically consistent geological cartography. In: Europlanet Science Congress 2020. https://doi.org/10.5194/epsc2020-1057 online, 21 September–9 Oct 2020, EPSC2020-1057.
Pohl, L., Britt, D.T., 2020. Strengths of meteorites. An overview and analysis of available data. Meteorit. Planet. Sci. 55 (4), 962–987. https://doi.org/10.1111/maps.13449.
Popescu, M., de León, J., Goldberg, H., Kovács, G., Ruggiu, L.K., Nagy, B., et al., 2024. Hyperspectral Imaging of Meteorites Using the HyperScout-H Instrument (No. EPSC2024-586). Copernicus Meetings. https://doi.org/10.5194/epsc2024-586.
Pugliatti, M., Rizza, A., Piccolo, F., Franzese, V., Bottiglieri, C., Giordano, C., et al., 2022. The Milani mission: overview and architecture of the optical-based GNC system. In: AIAA Scitech 2022 Forum, p. 2381. https://doi.org/10.2514/6.2022-2381.
Raducan, S.D., Jutzi, M., Cheng, A.F., Zhang, Y., Barnouin, O., Collins, G.S., et al., 2024. Physical properties of asteroid Dimorphos as derived from the DART impact. Nat. Astron. 8 (4), 445–455. https://doi.org/10.1038/s41550-024-02200-3.
Riley, N.A., 1941. Projection sphericity. J. Sediment. Res. 11 (2), 94–95. https://doi.org/10.1306/D426910C-2B26-11D7-8648000102C1865D.
Rivkin, A.S., Chabot, N.L., Stickle, A.M., Thomas, C.A., Richardson, D.C., Barnouin, O., et al., 2021. The double asteroid redirection test (DART): planetary defense investigations and requirements. Planet. Sci. J. 2 (5), 173. https://doi.org/10.3847/PSJ/ac063e.
Robin, C.Q., Duchene, A., Murdoch, N., Vincent, J.B., Lucchetti, A., Pajola, M., et al., 2024. Mechanical properties of rubble pile asteroids (Dimorphos, Itokawa, Ryugu, and Bennu) through surface boulder morphological analysis. Nat. Commun. 15 (1), 6203. https://doi.org/10.1038/s41467-024-50147-w.
Rüsch, O., Bickel, V.T., 2023. Global mapping of fragmented rocks on the moon with a neural network: implications for the failure mode of rocks on airless surfaces. Planet. Sci. J. 4 (7), 126. https://doi.org/10.3847/PSJ/acd1ef.
Scheirich, P., Pravec, P., Meyer, A.J., Agrusa, H.F., Richardson, D.C., Chesley, S.R., et al., 2024. Dimorphos orbit determination from mutual events photometry. Planet. Sci. J. 5 (1), 17. https://doi.org/10.3847/PSJ/ad12cf.
Shukla, M.K., Sharma, A., 2018. A brief review on breccia: it's contrasting origin and diagnostic signatures. Solid Earth Sci. 3 (2), 50–59. https://doi.org/10.1016/j.sesci.2018.03.001.
Spray, J.G., 2016. Lithification mechanisms for planetary regoliths: the glue that binds. Annu. Rev. Earth Planet. Sci. 44 (1), 139–174. https://doi.org/10.1146/annurev-earth-060115-012203.
Sugimoto, C., Tatsumi, E., Cho, Y., Morota, T., Honda, R., Kameda, S., et al., 2021. High-resolution observations of bright boulders on asteroid Ryugu: 1. Size frequency distribution and morphology. Icarus 369, 114529. https://doi.org/10.1016/j.icarus.2021.114529.
Sugita, S., Honda, R., Morota, T., Kameda, S., Sawada, H., Tatsumi, E., et al., 2019. The geomorphology, color, and thermal properties of Ryugu: implications for parent-body processes. Science 364 (6437), eaaw0422.
Tamas, C.G., Milési, J.P., 2003. Hydrothermal breccia pipe structures–general features and genetic criteria–II. Phreatic breccias. Studia Univ. Babes-Bolyai Geol. 48 (1), 55–66.
Thomas, C.A., Naidu, S.P., Scheirich, P., Moskovitz, N.A., Pravec, P., Chesley, S.R., et al., 2023. Orbital period change of Dimorphos due to the DART kinetic impact. Nature 616 (7957), 448–451.
Turner, F.J., 1948. Mineralogical and Structural Evolution of the Metamorphic Rocks, vol. 30. Geological Society of America.
Tusberti, F., Pajola, M., Munaretto, G., Penasa, L., Lucchetti, A., Beccarelli, J., et al., 2024a. Ice degradation and Boulder size frequency distribution analysis of the fresh Martian crater S1094b. Icarus 423, 116255. https://doi.org/10.1016/j.icarus.2024.116255.
Tusberti, F., Massironi, M., Pozzobon, R., Penasa, L., 2024b. Geologic evolution and map of Copernicus crater interior (moon). Geol. Field Trips Maps 16 (1.1), 1–19. https://doi.org/10.3301/GFT.2024.01.
Wadell, H., 1932. Volume, shape, and roundness of rock particles. J. Geol. 40 (5), 443–451. https://doi.org/10.1086/623964.
Wadell, H., 1933. Sphericity and roundness of rock particles. J. Geol. 41 (3), 310–331. https://doi.org/10.1086/624040.
Wadell, H., 1935. Volume, shape, and roundness of quartz particles. J. Geol. 43 (3), 250–280. https://doi.org/10.1086/624298.
Watanabe, S.I., Tsuda, Y., Yoshikawa, M., Tanaka, S., Saiki, T., Nakazawa, S., 2017. Hayabusa2 mission overview. Space Sci. Rev. 208, 3–16.
Weiss, B.P., Elkins-Tanton, L.T., 2013. Differentiated planetesimals and the parent bodies of chondrites. Annu. Rev. Earth Planet. Sci. 41 (1), 529–560. https://doi.org/10.1146/annurev-earth-040610-133520.
Zinzi, A., Hasselmann, P.H.A., Della Corte, V., Deshapriya, J.D.P., Gai, I., Lucchetti, A., et al., 2024. VADER: probing the dark side of Dimorphos with LICIACube LUKE. Planet. Sci. J. 5 (4), 103. https://doi.org/10.3847/PSJ/ad3826.